Supporting Information for "4D Physics-Based Pore Pressure Monitoring Using Passive Image Interferometry"

Eldert Fokker[1,2], Elmer Ruigrok[1,2], Rhys Hawkins[1,3], Jeannot Trampert[1]

[1]Department of Earth Sciences, Utrecht University, Princetonlaan 8a, 3584 CB, Utrecht, the Netherlands

[2]R&D Seismology and Acoustics, Royal Netherlands Meteorological Institute, Utrechtseweg 297, 3731 GA, De Bilt, the Netherlands

[3]Now at: School of Computing and Research School of Earth Sciences, Australian National University, Acton ACT 2601, Australia

Corresponding author: Eldert Fokker, e.b.fokker@uu.nl

Contents of this file

Figures S1 to S7

References

Dinoloket. (2022). *Groundwater research; borehole identification B08C0952.* `https://www.dinoloket.nl/en/subsurface-data`. (Last accessed: 7 September 2022)

Fokker, E., Ruigrok, E., Hawkins, R., & Trampert, J. (2021). Physics-based relationship for pore pressure and vertical stress monitoring using seismic velocity variations. *Remote Sensing*, *13*(14), 2684. doi: 10.3390/rs13142684

Grondwatertools. (2022). `https://www.grondwatertools.nl/gwsinbeeld/`. (Last accessed: 7 September 2022)

Kruiver, P. P., Van Dedem, E., Romijn, R., de Lange, G., Korff, M., Stafleu, J., ... others (2017). An integrated shear-wave velocity model for the Groningen gas field, the Netherlands. *Bulletin of Earthquake Engineering*, *15*(9), 3555–3580. doi: 10.1007/s10518-017-0105-y

Romijn, R. (2017). *Groningen velocity model 2017* (Tech. Rep.). Assen, the Netherlands: Nederlandse Aardolie Maatschappij NV. Retrieved from `https://nam-feitenencijfers.data-app.nl/download/rapportdialog/9a5751d9-2ff5-4b6a-9c25-e37e76976bc1`

Sens-Schönfelder, C., & Wegler, U. (2006). Passive image interferometry and seasonal variations of seismic velocities at Merapi Volcano, Indonesia. *Geophysical Research Letters*, *33*(21). doi: 10.1029/2006GL027797

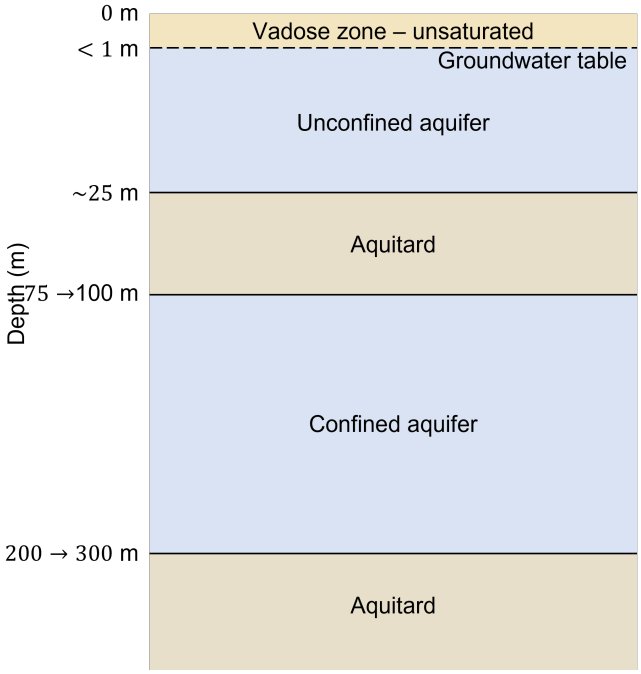

Figure S1. Schematic overview of the hydrologic layering. In the first 25 m we find an unconfined aquifer, where the groundwater table is situated at a depth smaller than 1 m. From 25 m to roughly 75-100 m, we find an aquitard, consisting of impermeable clay layers. From 75-100 m to 200-300 m depth we find a confined aquifer.

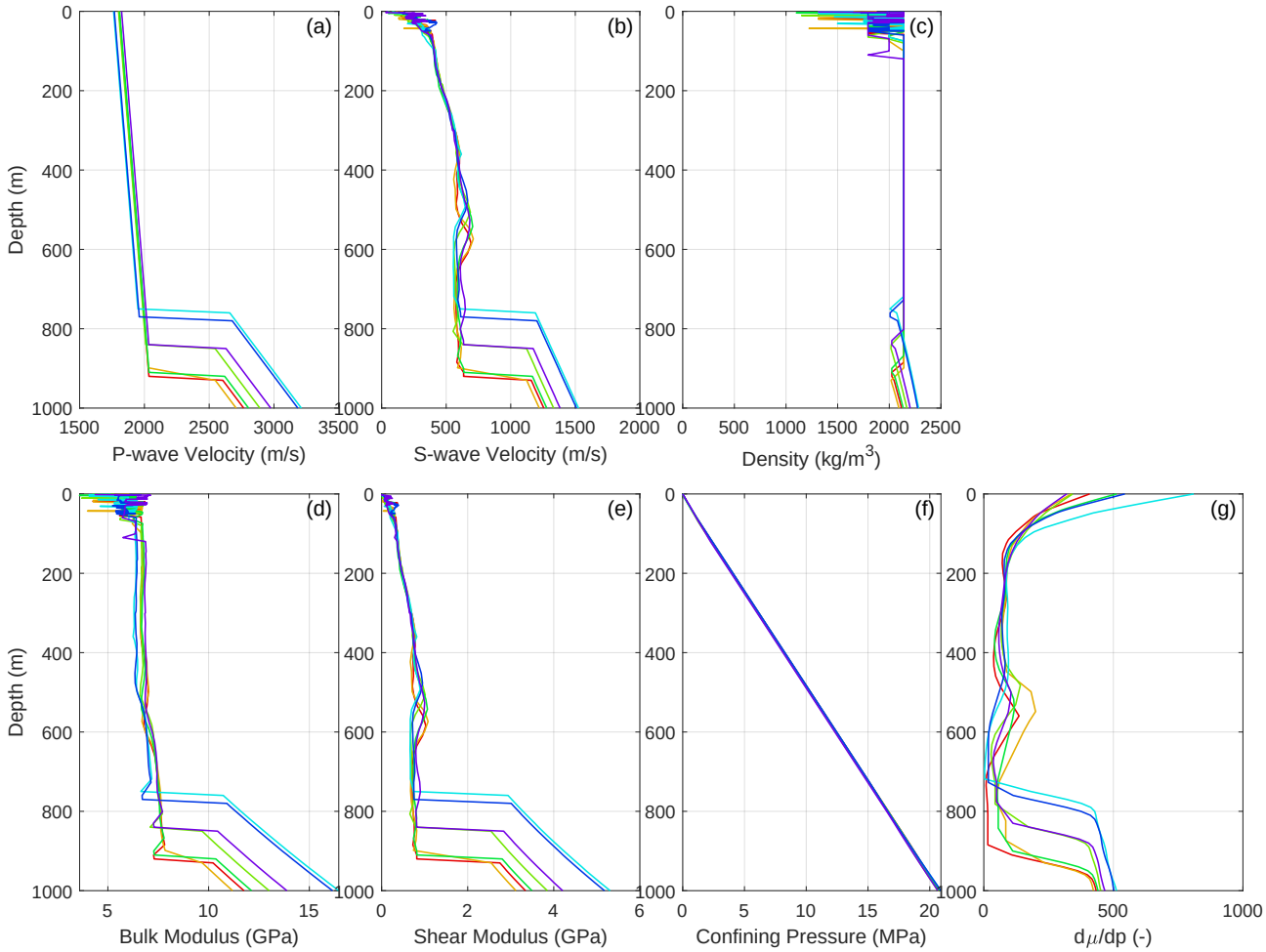

Figure S2. Elastic models from Kruiver et al. (2017) and Romijn (2017) for the regions indicated by the colored circles in Figure 1: (a) Compressional-wave velocity v_p, (b) shear-wave velocity v_s, (c) mass density ρ, (d) bulk modulus $\kappa = \rho v_p^2 - \frac{4}{3}\rho v_s^2$, (e) shear modulus $\mu = \rho v_s^2$, (f) confining pressure $P = \int_0^z \rho(z) g \, dz$, with g the gravitational acceleration and z the depth below surface, and (g) pressure derivative of the shear modulus $\mu' = d\mu/dp$, based on the smoothed derivative of the shear modulus with respect to confining pressure.

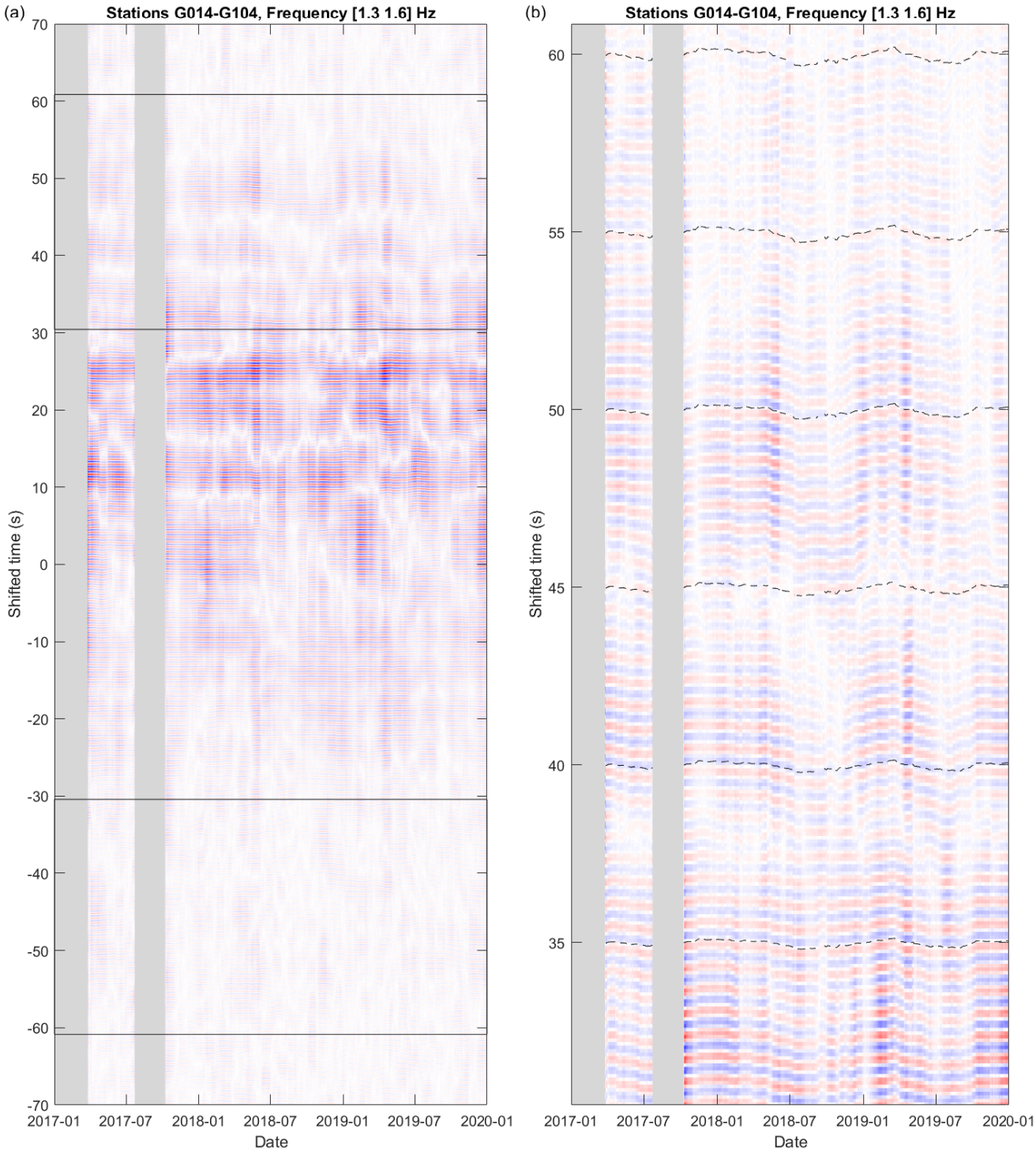

Figure S3. Cross-coherence of seismic noise recorded at receivers G014 and G104 at frequency range [1.3 1.6] Hz. (a) Cross-coherence for shifted times between -70 and +70 seconds, indicating in black the time-window used to retrieve relative velocity changes. (b) Zoomed cross-coherence at the causal time window plotted in (a), showing consistent arrivals up to 60 seconds. The black dashed curves indicate waveform stretching for which the correlation with the reference is highest (equation 2). This corresponds to the relative velocity variations between receivers G014 and G104. For this particular receiver pair, the anti-causal part is weak in this frequency range.

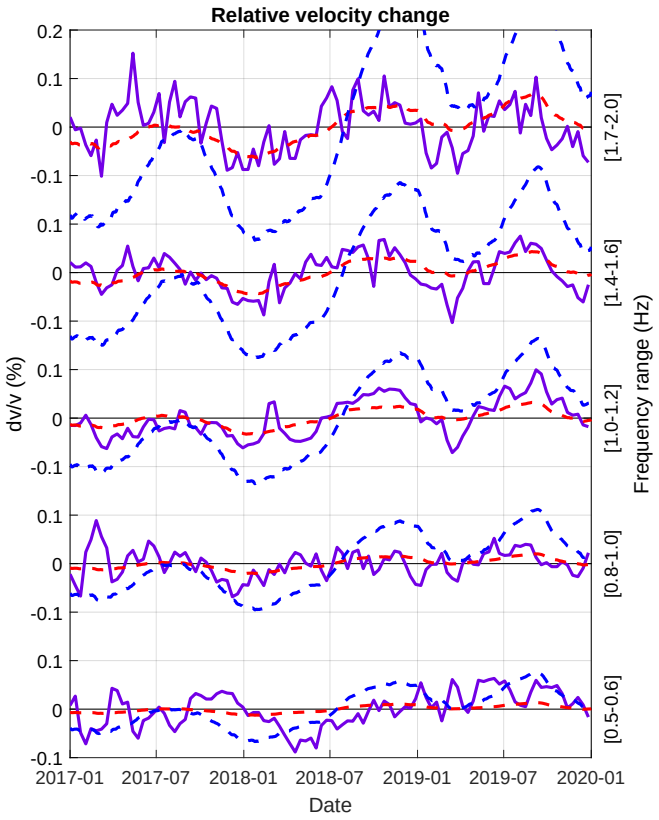

Figure S4. Models and observations of seismic velocity changes for the region indicated in Figure 1 in purple. The purple curves represent the velocity changes for six frequency ranges estimated using passive image interferometry (Sens-Schönfelder & Wegler, 2006) on the vertical components, while the red and the blue dashed curves show respectively the fundamental mode Rayleigh- and Love-wave velocity changes as modelled (Fokker et al., 2021) from pore pressure observations at the borehole piezometer (Fig. 1, blue point; Dinoloket, 2022).

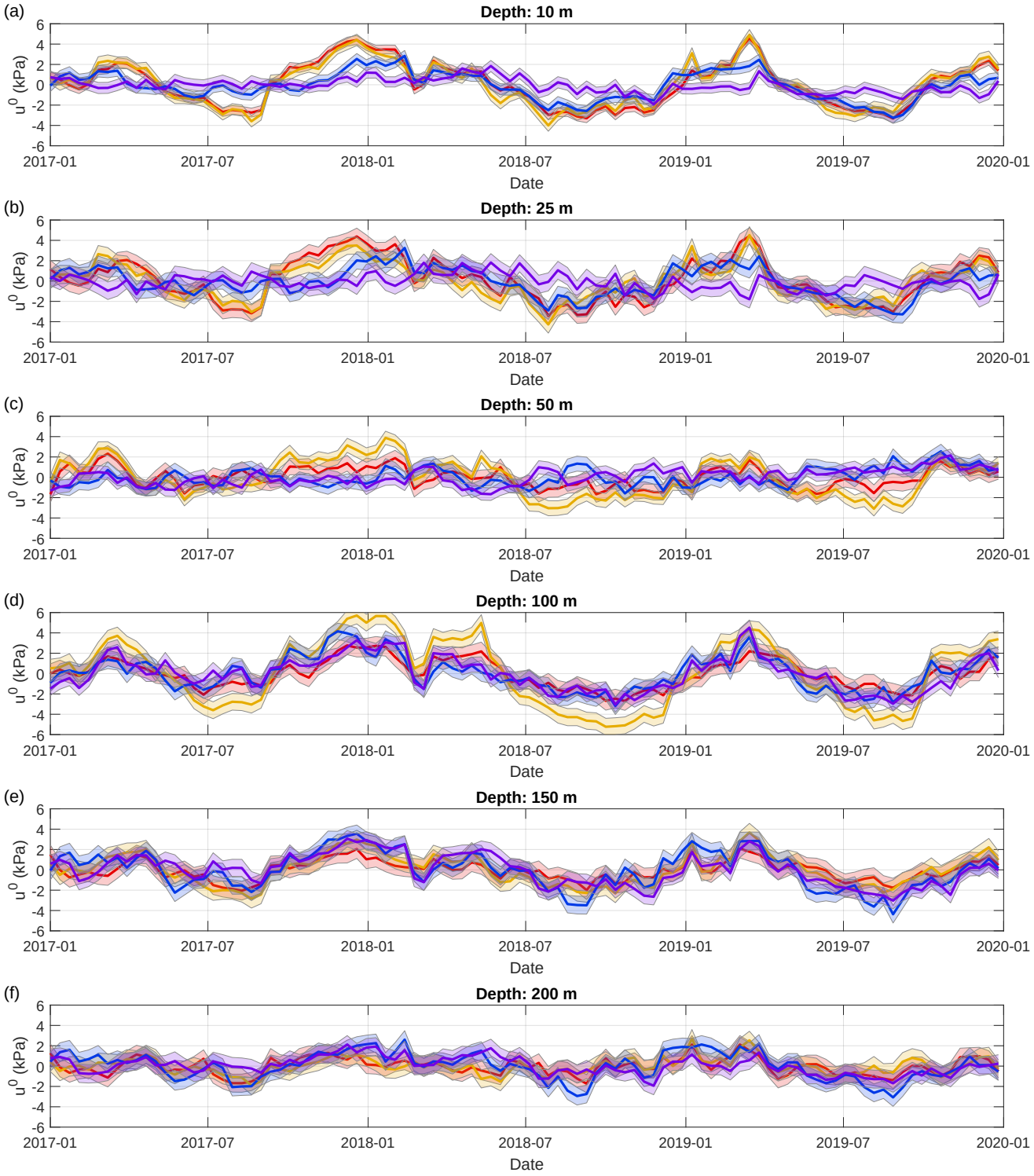

Figure S5. Comparison between pore pressure variations as modelled for different regions and depths. The pore pressure change has been modelled using Equations 12 and 7 (solid lines; colors correspond to regions in Fig. 1), while the uncertainty range was modelled using the squareroot of the diagonal of the posterior model covariance (Eq. 15; Fig. 3g). The uncertainty ranges of the shallow models in the northwest and the southeast do not overlap, indicating a significant difference. Lateral variations of deeper pore pressure models, however, fall within the uncertainty and can therefore not be classified as significant.

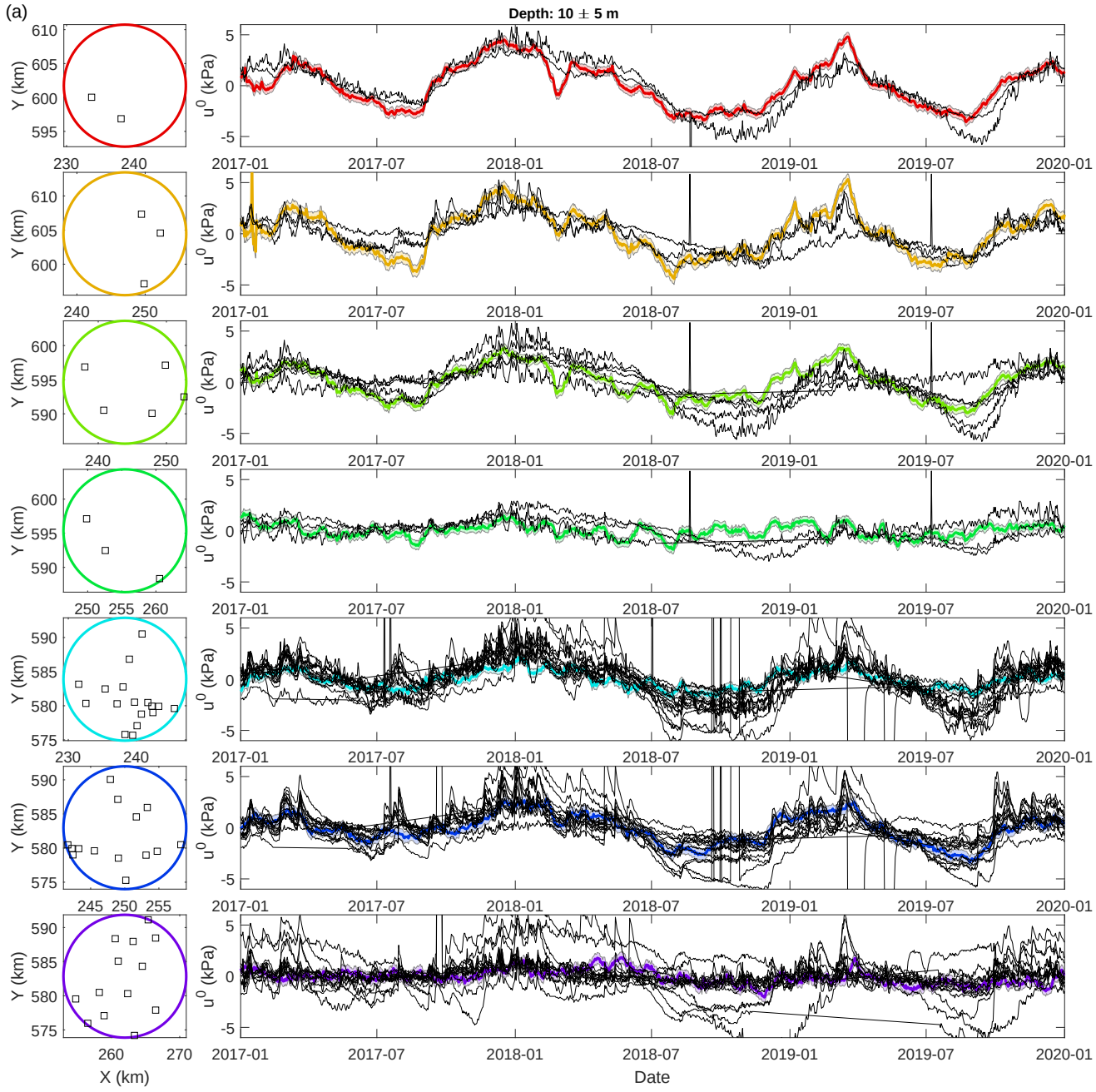

Figure S6. (cont.)

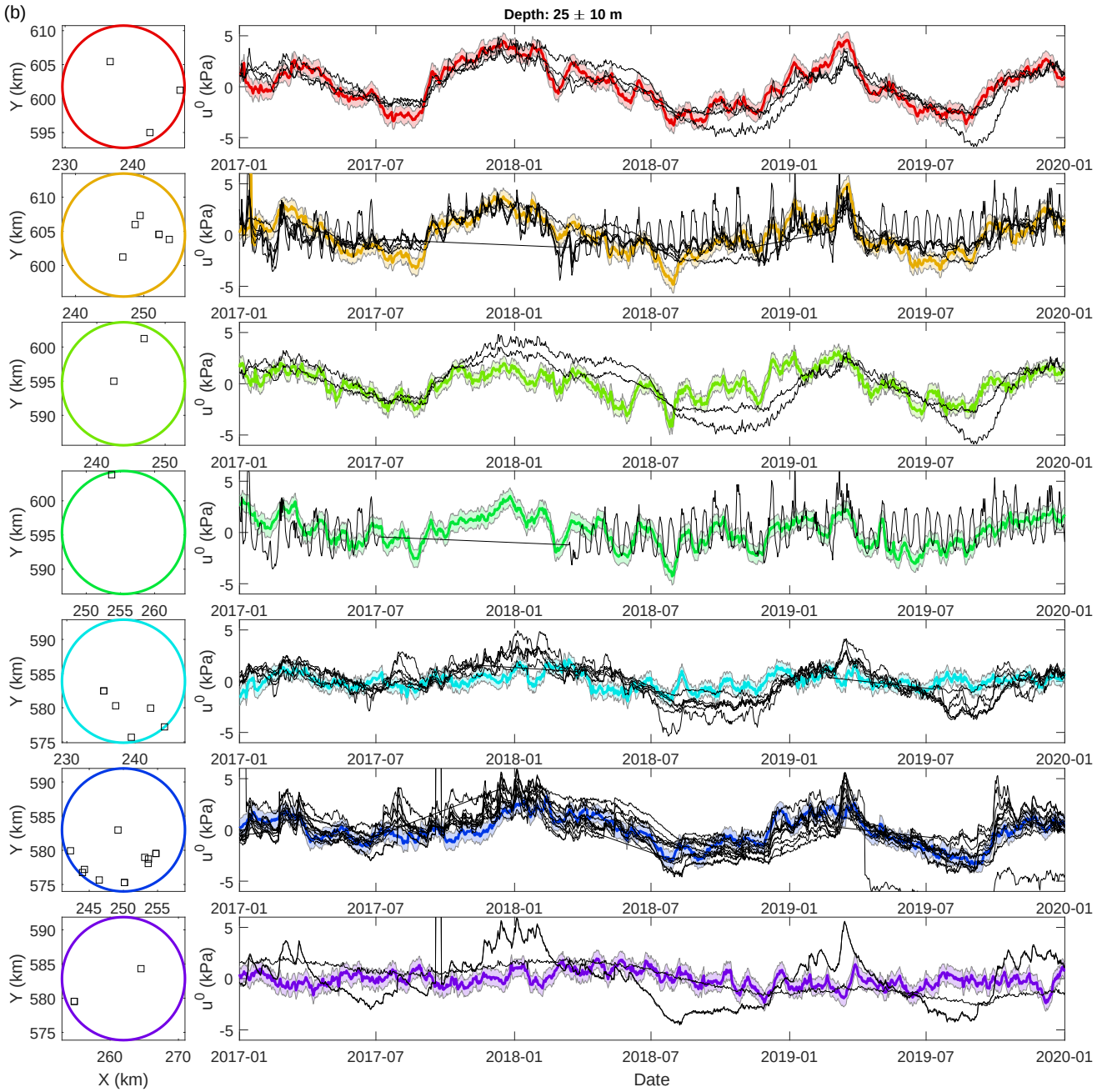

Figure S6. Comparison between pore pressure variations as modelled in this study and measured by local shallow piezometers (*Grondwatertools*, 2022). Left: Map views of separate regions in accordance with Figure 1, indicating locations of the piezometers as black squares. Right: Pore pressure variations as modelled in accordance with Section 5 for the region shown on the left, and measurements of pore pressure change (black) at the locations of the piezometers shown on the left. The pore pressure models are shown for depths of (a) 10 m and (b) 25 m, whereas the piezometric measurements are obtained (a) between 5 and 15 m depth and (b) between 15 and 35 m depth.

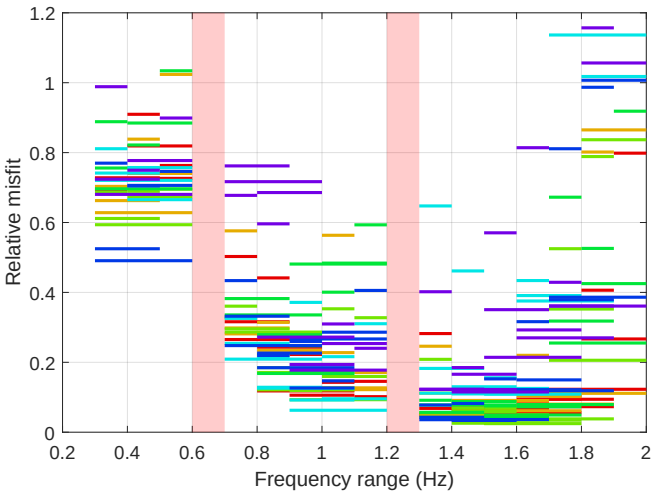

Figure S7. Relative misfit $\Phi = \frac{\sum_t (dv/v(\omega,t) - G\tilde{m}(\omega,t))^2}{\sum_t (dv/v(\omega,t))^2}$ between measured velocity change dv/v and predicted velocity change based on the inferred pore pressure model $G\tilde{m}$. The different colors correspond to the regions in Figure 1. The frequencies in the pink band were excluded.